LAWRENCE
LIVERMORE
NATIONAL
LABORATORY

LLNL-JRNL-753799

Paper submitted to EPSL

S. M. Elardo, A. Shahar, T. D. Mock, C. K. Sio

June 27, 2018

Earth and Planetary Science Letters

Disclaimer

The Effect of Core Composition on Iron Isotope Fractionation between Planetary Cores and Mantles

Stephen M. Elardo[1,2,*], Anat Shahar[1], Timothy D. Mock[3], and Corliss K. Sio[1,4]

[1]Geophysical Laboratory, Carnegie Institution of Washington, Washington, DC 20015, USA

[2]Department of Geological Sciences, University of Florida, Gainesville, FL 32611, USA

[3]Department of Terrestrial Magnetism, Carnegie Institution of Washington, Washington, DC 20015, USA

[4]Nuclear and Chemical Sciences Division, Lawrence Livermore National Laboratory, Livermore, CA 94550, USA

*Author to whom correspondence should be addressed: selardo@ufl.edu

ABSTRACT

We have conducted high-pressure, high-temperature isotope exchange experiments between molten silicate and molten Fe-Si-C-alloys to constrain the effect of Si on equilibrium Fe isotope fractionation during planetary core formation. The values of $\Delta^{57}Fe_{Metal\text{-}Silicate}$ at 1850 °C and 1 GPa determined by high-resolution MC-ICP-MS in this study range from -0.013 ± 0.054‰ (2SE) to 0.072 ± 0.085‰ with 1.34 – 8.14 atom % Si in the alloy, respectively. These results, although not definitive on their own, are consistent with previous experimental results from our group and a model in which elements that substitute for Fe atoms in the alloy structure (i.e., Ni, S, and Si) induce a fractionation of Fe isotopes between molten silicate and molten Fe-alloys during planetary differentiation. Using *in situ* synchrotron X-ray diffraction data for molten Fe-rich alloys from the literature, we propose a model to explain this fractionation behavior in which impurity elements in Fe-alloys cause the nearest neighbor atomic distances to shorten, thereby stiffening metallic bonds and increasing the preference of the alloy for heavy Fe isotopes relative to the

silicate melt. This fractionation results in the bulk silicate mantles of the smaller terrestrial planets and asteroids becoming isotopically light relative to chondrites, with an enrichment of heavy Fe isotopes in their cores, consistent with magmatic iron meteorite compositions. Our model predicts a bulk silicate mantle δ^{57}Fe ranging from -0.01‰ to -0.12‰ for the Moon, -0.06‰ to -0.33‰ for Mars, and -0.08‰ to -0.33‰ for Vesta. Independent estimates of the δ^{57}Fe of primitive mantle source regions that account for Fe isotope fractionation during partial melting agree well with these ranges for all three planetary bodies and suggest that Mars and Vesta have cores with impurity (i.e., Ni, S, Si) abundances near the low end of published ranges. Therefore, we favor a model in which core formation results in isotopically light bulk silicate mantles for the Moon, Mars, and Vesta. The processes of magma ocean crystallization, mantle partial melting, and fractional crystallization of mantle-derived melts are all likely to result in heavy Fe isotope enrichment in the melt phase, which can explain why basaltic samples from these planetary bodies have variable δ^{57}Fe values consistently heavier than our bulk mantle estimates. Additionally, we find no clear evidence that Fe isotopes were fractionated to a detectable level by volatile depletion processes during or after planetary accretion, although it cannot be ruled out.

Keywords: Core formation, iron isotopes, experimental petrology, isotope geochemistry, mantle, planetary science.

1.0 - INTRODUCTION

The ubiquity of Fe in the three major geochemical reservoirs in terrestrial planets – cores, mantles, and crusts – makes the Fe isotope system potentially powerful for understanding planetary differentiation. The Fe isotope compositions of planetary sample suites show significant variations relative to the narrow range found in chondrites, the average of which is $\delta^{57}Fe = \sim 0$ ‰ (relative to IRMM-014; Craddock and Dauphas, 2011), which implies that fractionations were produced by processes during and/or after planetary accretion. Magmatic iron meteorites almost ubiquitously have Fe isotope compositions that are heavy relative to chondrites, with $\delta^{57}Fe$ values ranging from close to chondritic up to 0.32‰ (Poitrasson et al., 2005; Williams et al., 2006). Although non-magmatic iron meteorites span a similar range in compositions, we do not consider them further as they are likely not the direct products of core formation, but rather other processes such as collisional heating. Interestingly, planetary silicate reservoirs span a similar range. Basaltic shergottites and non-cumulate eucrites, lavas from Mars and Vesta, respectively, both range from slightly negative to positive $\delta^{57}Fe$ values (Poitrasson et al., 2004; Weyer et al., 2005; Schoenberg and von Blanckenburg, 2006; Wang et al., 2012; Sossi et al., 2016a). Lunar basalts span a comparatively large range, from slightly negative values in volcanic glasses to very heavy values in high-Ti mare basalts (Poitrasson et al., 2004; Weyer et al., 2005). Terrestrial mantle xenoliths span a large range from roughly -0.8‰ to 0.2‰, in part due to the effects of metasomatism, alteration, and melt extraction (Weyer and Ionov, 2007; Zhao et al., 2010; Craddock et al., 2013; Poitrasson et al., 2013; Williams and Bizimis, 2014). However, a prominent peak in the global peridotite dataset close to the chondritic value provides evidence that Earth's upper mantle has a $\delta^{57}Fe$ near chondrites (see review by Dauphas et al., 2017). Mid-ocean ridge basalts (MORBs) are ubiquitously fractionated to fairly homogenous $\delta^{57}Fe$ of ~0.15‰, which is generally thought to be

caused by partial melting (Williams et al., 2005; Weyer and Ionov, 2007; Craddock et al., 2013; Teng et al., 2013; Dauphas et al., 2014).

The differences in Fe isotope systematics between planetary samples have been attributed to various mechanisms. Crystal/liquid fractionation during fractional crystallization and mantle melting plays a role in generating the variability observed in lunar basalts, shergottites, and the abyssal peridotite-MORB offset (Weyer and Ionov, 2007; Craddock et al., 2013; Dauphas et al., 2014; Sossi et al., 2016a). However, the two fractionation mechanisms most frequently discussed are volatile depletion and core formation. The debate between these two mechanisms is largely a product of uncertainty regarding the δ^{57}Fe of bulk planetary mantles and the paucity of experimentally-determined fractionation factors between silicate minerals and melts, metallic melts, and vapors. There has been significant debate over whether core-mantle equilibration during planetary differentiation results in Fe isotope fractionation (Poitrasson et al., 2009; Hin et al., 2012; Shahar et al., 2015; 2016; Elardo and Shahar, 2017; Liu et al., 2017) and how important this effect is relative to other mechanisms (e.g., Poitrasson et al., 2004; Weyer et al., 2005; Schoenberg and von Blanckenburg, 2006; Poitrasson, 2007; Williams et al., 2012; Sossi et al., 2016a; 2016b). Our previous work has shown that Fe alloying with siderophile elements such as S and Ni results in Fe isotope fractionation during metal-silicate equilibration (Shahar et al., 2015; Elardo and Shahar, 2017), but a more complete picture of the compositional effects on and causes of this fractionation has been lacking. Here we present new experimental data on the effects of Si in planetary cores on Fe isotope fractionation between metal and silicate, and we examine (1) the cause of metal-silicate fractionation of Fe isotopes observed in the broader experimental literature from a metallic structure perspective, (2) the discrepancies in results between previous low-pressure experimental

92 work (Poitrasson et al., 2009; Hin et al., 2012) and our own, and (3) the implications of this
93 fractionation for the Fe isotope compositions of planetary mantles.
94
95 **2.0 - EXPERIMENTAL AND ANALYTICAL METHODS**
96 **2.1 – Piston-Cylinder Experiments**
97 Iron isotope exchange experiments were conducted at the Geophysical Laboratory (GL),
98 Carnegie Institution of Washington. The silicate composition (Table 1) was the same ^{54}Fe spiked
99 peridotite mix used by Elardo and Shahar (2017) and similar to that used by Shahar et al. (2015).
100 Starting metal compositions were $Fe_{91}Si_9$ and $Fe_{95.5}Si_{4.5}$. Starting materials had a bulk Earth-like
101 metal/silicate ratio (32 wt. % metal) with the exception of PC 1529, which had ~20 wt. % metal.
102 Experiments were conducted using a ½ inch diameter Boyd-England-style end-loaded piston
103 cylinder. Experiments were run in talc-Pyrex cells with straight-walled graphite heaters at 1 GPa
104 and 1850 °C. Inner parts were MgO with the exception of the thermocouple sheath, which was
105 Al_2O_3. Stainless steel base plugs were enclosed by pyrophyllite sheaths. All MgO inner parts were
106 dried at ~900 °C for at least 1 hour and were stored in a drying oven at ~105 °C. Starting materials
107 were loaded into high-purity graphite and were stored in a desiccated drying oven at ~105 °C
108 typically for many days before use. Lead-foil and a MoS_2 suspension were used for lubrication
109 within the pressure vessel. Experiments were pressurized cold to a value ~1.25 GPa to promote a
110 more complete compression of the cell prior to heating. Pressure was added as the cell compressed
111 during heating to maintain the pressure of interest. Temperature was monitored with a type C
112 ($W_5Re_{95}/W_{26}Re_{74}$) thermocouple. Experimental durations ranged between 0.5 – 3 hours. Runs
113 were quenched by cutting power to the assembly and cooled to ~150 °C in ~10-15 seconds.
114

115 **2.2 – Silicon drift detector – energy dispersive spectrometry (SDD – EDS)**

116 A portion of each run product was mounted in epoxy and polished flat. The compositions
117 of the silicate and metal phases were determined via SDD-EDS analyses using the JEOL 6500F
118 field – emission scanning electron microscope at GL equipped with an Oxford X-Max 80 mm^2 Si
119 drift detector. Although traditional EDS analysis is semi-quantitative at best, SDD-EDS analysis
120 is equivalent to wavelength dispersive spectrometry analysis in both precision and accuracy for
121 major and most minor elements.

122 Samples were coated with Ir to a thickness of <1 nm. A sample of 99.995 % pure Fe metal was
123 re-polished and coated alongside each round of experiments for use as an analytical blank to assess
124 C surface contamination. After coating, all experiments and the C-blank were cleaned with an
125 Evactron 25/45 RF oxygen plasma cleaner immediately prior to SDD-EDS analyses to remove C
126 surface contamination; however, some surface C survived through to the analyses. Metal analyses
127 were made by collecting an SDD-EDS spectrum for 50s at operating voltage of 15 kV and a beam
128 current of 1 nA with a spot size of ~12 x 12 μm. Standards were pure Fe-metal, pure Ni metal, and
129 graphite. Two Fe metal samples, Si metal, and SiC were used as secondary standards. The amount
130 of C surface contamination was determined via analyses on the blank and the average C content
131 from these analyses was subtracted from the total C detected in analyses of experimental alloys,
132 typically resulting in analytical totals close to 100 wt. %. Silicate analyses were made using
133 quantitative mapping mode at 1 nA over an area of ~100 x 100 μm with a counting time of 1 ms
134 per pixel. Standards were pyrope, diopside, cossyrite, and Al-rich enstatite, and secondary
135 standards were a basaltic glass and San Carlos olivine.
136

2.3 – Multiple-Collector Inductively-Coupled Plasma Mass Spectrometry (MC-ICP-MS) Analyses

The remaining portion of each run product was crushed in an agate mortar and pestle. Metal and silicate phases were hand-picked under a binocular microscope and were easily discernible. Silicate separates were further purified with a strong magnet to ensure no contamination from small metal inclusions. Phase dissolutions and anion exchange chromatography procedures followed those of Craddock and Dauphas (2011). Phase separates and geostandards were dissolved in a three-step process: (1) 1 ml of concentrated HF + 0.5 ml of concentrated HNO_3, (2) 0.75 ml of concentrated HCl + 0.25 ml of concentrated HNO_3, and (3) 1 ml concentrated HCl + 0.5 ml concentrated HNO_3. During each step, solutions were kept in closed Savillex beakers on a hot plate at ~150 °C overnight and were then dried down before the addition of new acids. After step (3), the samples were dissolved in 0.5 – 5 ml of 6M HCl, depending on Fe concentration, for column chemistry. Iron was purified using 1 ml of BioRad AG-1X8 200 – 400 mesh pre-cleaned resin loaded in BioRad Poly-Prep columns. Between 0.1 and 0.5 ml of sample in 6M HCl was added to the columns and after elution of matrix elements, the sample was collected in 0.4M HCl. Purified Fe was then dried down, redissolved in 6M HCl, and the column chemistry was repeated with new resin. Afterward, purified Fe was dissolved in 5 ml of 0.3M HNO_3 for isotopic analysis.

Isotopic analyses were conducted in pseudo-high-resolution mode on the Nu Instruments Plasma II MC-ICP-MS at GL, which has a fixed array of 16 Faraday collectors each with a 10^{11} Ω amplifier. Samples and the standard (IRMM-524a) were analyzed at a concentration of ~2.5 – 4 ppm ^{56}Fe in 0.3M HNO_3 solutions. Instrumental mass fractionation was corrected for using sample-standard bracketing and interferences on $^{54}Fe^+$, $^{56}Fe^+$, and $^{57}Fe^+$ from ArN^+, ArO^+, and $ArOH^+$, respectively, were fully resolved using a 30 μm source slit and variable slits before the

electrostatic analyzer filter. Mass resolution of ~10,000 was estimated using ^{56}Fe. ^{53}Cr was measured simultaneously and the ^{54}Fe voltage was corrected for the ^{54}Cr interference. Samples were analyzed 10 - 20 times with each analysis consisting of 20 cycles of ~4 s integrations. Metal and silicate samples were always measured back to back on the same day.

3.0 – RESULTS

Experiments resulted in assemblages consisting of FeO-poor peridotite melt in equilibrium with molten Si-C-Fe-alloys (Fig. 1, Table 1). As expected, the Si-bearing starting metal compositions resulted in some reduction of FeO in the silicate melt and the oxidation of Si^0. The FeO contents of peridotite melts in our experiments ranged from 0.47 to 0.90 wt. %. The Fe-alloys contained between 0.82 and 4.95 wt. % Si (1.34 – 8.14 atom % Si). Similar chemical compositions of metal and silicate melts across similar experiments of different durations (Table 1) indicated that 30 minutes was sufficient to reach chemical equilibrium.

Isotopic equilibrium was tested with the three-isotope exchange method (Shahar et al., 2008; 2017) and a time series. For each experiment reported here, both silicate and metal fractions had the identical $\Delta^{56}Fe$ values (i.e., departures from mass-dependency) within analytical error, indicating they lie on the same secondary mass fractionation line (Table 2). Additionally, three experiments ranging in duration from 0.5 to 2 hours resulted in identical $\Delta^{57}Fe_{Metal\text{-}Silicate}$ within analytical error. Therefore, we conclude that the experiments reported here closely approached isotopic equilibrium. Two recent studies have argued that complex kinetic pathways to equilibrium in three isotope exchange experiments would create difficulties in determining the correct equilibrium fractionation factor between two phases (Cao and Bao, 2017; Bourdon et al., 2018); however, such concerns are only relevant for studies in which an extrapolation to a secondary

fractionation line using a series of unequilibrated experiments is used and are thus not relevant for our group's work. The Fe isotopic fractionation between metal and silicate (i.e., $\Delta^{57}Fe_{Metal\text{-}Silicate} = \delta^{57}Fe_{Metal} - \delta^{57}Fe_{Silicate}$) for these experiments range between -0.013 ± 0.054‰ (2SE) and 0.072 ± 0.085‰ (Fig. 2, Table 2). Analyses of the AGV-2, BIR-1, and BHVO-2 geostandards were similar to accepted values.

4.0 – DISCUSSION

4.1 – Does Si in Planetary Cores Have an Effect on Fe Isotope Fractionation at Low Pressure?

The results of our experiments containing Si-Fe-alloys are consistent with previous results from our group for experiments with S- and Ni-Fe alloys (Fig. 3), but with the exception of one experiment, do not show resolvable effects on their own. The $\Delta^{57}Fe_{Metal\text{-}Silicate}$ at 1850 °C of the experiment containing the most Si-rich metal is the highest among our Si-bearing experiments. The fractionation is 0.072 ± 0.085‰ and falls on the trend in the Ni- and S-bearing experiments (Fig. 3), although this experiment is not resolved from 0‰. These results do not definitely demonstrate an effect attributable to Si. However, their consistency with previous experiments combined with the observations Fe isotope fractionation between silicates and Si-Fe metal in aubrite meteorites (Jordan et al., 2019) suggests that experiments with higher Si in Fe alloys may follow the behavior suggested by Elardo and Shahar (2017) wherein elements that substitute for Fe in the alloy structure drive Fe isotope fractionation. As only one of the Si-bearing experiments had a $\Delta^{57}Fe_{Metal\text{-}Silicate}$ at 1850 °C greater than 0‰ outside of uncertainty, it is difficult to draw any definitive conclusions from this dataset alone. Experiments with greater amounts of Si in the alloy were attempted but are not reported due to the large analytical uncertainties on the isotopic compositions of the silicate fractions. The recovery of sufficient metal-free silicate to enable robust

206 analyses was extremely challenging due to the low FeO abundances in the melt. In sections below,
207 we will consider the new Si-bearing experiments alongside previous experiments from our group
208 and others in an attempt to elucidate the causes of Fe isotopic fractionation behavior and its
209 consequences for the smaller terrestrial planets and asteroids.
210
211 **4.2 – Iron Isotope Fractionation During Core Formation: A Metallic Structural Effect?**
212 The structures of metallic liquids offer insights into the Fe isotopic fractionation behavior
213 observed in experiments. Core-relevant metallic liquids with and without light elements (i.e., S,
214 Si, C) have been studied *in situ* using synchrotron X-ray diffraction (e.g., Sanloup et al., 2000;
215 2002; 2004; Kono et al., 2015; Shibazaki et al., 2015). Radial distribution functions derived from
216 these measurements have shown that Fe-rich metallic liquids retain short- to medium-range order
217 and allow for the determination of nearest neighbor atomic distances (r_1). This is potentially
218 insightful for isotopic studies, as bond stiffness affects a phase's preference for light vs. heavy
219 isotopes of an element, with shorter, stiffer bonds generally favoring heavy isotopes (e.g., Young
220 et al., 2015).
221 Between ambient pressure and ~5 GPa, and ~1200 to 2000 °C, r_1 is not strongly dependent on
222 either pressure or temperature, but it does exhibit a correlation with composition. Nearest neighbor
223 distances in molten alloys decrease linearly from ~2.58 to ~2.51 Å with increasing abundances of
224 alloying elements from 0 to ~40 at. % (Fig. 4). Similar to $\Delta^{57}Fe_{Metal\text{-}Silicate}$ values (Fig. 3), the r_1
225 distances of molten Fe-rich alloys appear to be dependent on the total abundance of impurity
226 elements in the molten Fe-alloy, independent of the identity of the elements within the resolution
227 of the measurements. Therefore, we suggest that shortening of Fe bonds in molten Fe alloys due
228 to the addition of alloying elements may be the primary mechanism for our observed Fe isotope

fractionation behavior. This effect would be directly relevant to core-mantle equilibration in the Moon, Mercury, differentiated asteroids such as Vesta, and low-pressure core formation on Mars. There appears to be a structural transition in molten Fe-alloys at ~5 GPa, near the bcc-fcc-liquid triple point (Sanloup et al., 2000; Kono et al., 2015; Shibazaki et al., 2015). It is unclear what effect this structural transition will have on Fe isotope fractionation; however, we note that the transition results in further shortening of r_1, so it is possible that pressures > 5 GPa could enhance Fe isotope fractionation. This model is not without some assumptions and complexities that require experimental verification. We assume that Ni has the same effect on r_1 as S, C, and Si. To our knowledge, there are no similar studies on the effect of Ni on r_1 in Fe-rich alloys. However, the r_1 distance in pure molten Ni (~2.48 – 2.49 Å; Schenk et al., 2002) is shorter than that in pure Fe, so this assumption may be valid.

4.3 – Substitutional vs. Interstitial Element Partitioning

Elardo and Shahar (2017) proposed that elements which substitute for Fe in the alloy structure, such as Ni, S, and Si, have a greater effect on the bonding environment of Fe atoms and the magnitude of Fe isotope fractionation than elements such as C and N, which partition into interstitial sites in the Fe-alloy. This model is supported by a few lines of evidence. The expectation from first principles is that metals should favor heavy Fe isotopes relative to silicates. Metallic bonds have delocalized, itinerant electrons which form shorter and stiffer bonds than localized electrons, and thus metallic bonds should favor heavy Fe isotopes over Fe-O bonds in silicates (Young et al., 2015). However, if we regress the metallic compositional effect on $\Delta^{57}Fe_{Metal\text{-}Silicate}$ in terms of the total amount of impurities in the metal, we would predict that the $\delta^{57}Fe$ of pure Fe should be significantly lighter than silicate melt by >0.2‰ at 1850 °C (Fig. 3a). This regression

would also predict a sign change in $\Delta^{57}Fe_{Metal\text{-}Silicate}$ at ~18 at. % total impurities, which has no foundation in theory. Alternatively, if we regress the metallic compositional effect in terms of the total amount of only substitutional impurities (Fig. 3b), we predict no sign change and that all Fe-alloys should be heavier than silicate melt, in line with the expectations from first principles. At 1850 °C, the compositional effect of substitutional impurities can be expressed by following relationship:

$$\Delta^{57}Fe_{Metal-Silicate} = 0.0120 * X_{Sub} + 0.0176,\ R^2 = 0.89 \qquad (Eq.1)$$

where X_{Sub} is the total at. % of substitutional elements (i.e., Ni, S, and Si) in the metal phase. This regression includes all experiments in Fig. 3 with the exception of the Fe-C set, which contain no substitutional impurities in the Fe alloys. We can also parameterize $\Delta^{57}Fe_{Metal\text{-}Silicate}$ to include the effect of temperature, as equilibrium stable isotope fractionation scales as $1/T^2$:

$$\Delta^{57}Fe_{Metal-Silicate} = \frac{5.41 * 10^4 * X_{Sub} + 7.93 * 10^4}{T^2} \qquad (Eq.2)$$

where T is temperature in K. Interestingly, the effects of individual element impurities on $\Delta^{57}Fe_{Metal\text{-}Silicate}$ are more tightly correlated in the substitutional-only regression than in the all-impurity regression (Fig. 3b). This is consistent with the data presented in Fig. 4, which shows that all impurities in Fe alloys have essentially the same effect on nearest neighbor distance in the alloy. Therefore, we conclude that Equation 2 most accurately describes the effects of composition and temperature on the magnitude of Fe isotope fractionation between molten Fe-rich metal and molten peridotite based on currently available data. This is also consistent with the compositions of

magmatic iron meteorites, which are nearly ubiquitously heavy (Poitrasson et al., 2005; Williams et al., 2006), with metal – silicate fractionation observed in aubrite meteorites that contain Si-Fe-alloys (Jordan et al., 2019), and with the fractionation observed in pallasite meteorites (Poitrasson et al., 2005).

A complexity in this model is that the presence of C in Fe-alloys also appears to shorten nearest neighbor distances with a similar effect to S and Si (Fig. 4), yet apparently does not have a corresponding effect on Fe isotope fractionation. The reason for this behavior is unknown and more work is needed to further investigate the effects of interstitial elements.

4.4 – Reconciling Differing Experimental Results from the Literature

Groups investigating equilibrium Fe isotope fractionation during core formation have come to disparate conclusions using similar techniques. Using piston-cylinder and multi-anvil experiments, Poitrasson et al. (2009) and Hin et al. (2012) argued that metal-silicate equilibration does not result in a resolvable fractionation of Fe isotopes. Conversely, Shahar et al. (2015) and Elardo and Shahar (2017) found resolvable, relatively large fractionations that correlated with the composition of the metal phase. Here we attempt to reconcile these observations.

Poitrasson et al. (2009) presented the results of seven experiments designed to investigate Fe isotope fractionation. Their starting materials consisted of a devolatilized chondrite composition with one exception in which S was not present in the system. Six of the seven experiments were conducted at 2000 °C and ranged in pressure from 2 – 7.7 GPa, with durations between < 2 minutes and 10 minutes. The average $\Delta^{57}Fe_{Metal\text{-}Silicate}$ of those six experiments was 0.047 ± 0.063‰, despite the fact that the Fe alloys contained Ni and S.

297 The seventh experiment from Poitrasson et al. (2009) is informative in resolving this
298 discrepancy. That experiment (PC-564b) was conducted at 1750 °C, 1 GPa, and most importantly,
299 at 30 minutes it was their longest duration experiment. The bulk metal phase consisted of a C-rich
300 Fe-Ni-S melt. An immiscible S-rich Fe-Ni-C melt was also present; however, the C-rich melt was
301 far more abundant so it likely controlled the measured metal composition. Although Poitrasson et
302 al. (2009) did not discuss the results of this experiment in detail, it yielded a $\Delta^{57}Fe_{Metal\text{-}Silicate}$ of
303 0.134 ± 0.101‰ and is their only fractionation factor resolved from 0‰. This value agrees well
304 with our group's results (Fig. 3). Shahar et al. (2015) showed that an experiment conducted for 5
305 minutes at 1650 °C and 1 GPa did not come to isotopic equilibrium, as revealed by the three-
306 isotope exchange method. Furthermore, Shahar et al. (2008) demonstrated that chemical
307 equilibrium is reached faster than isotopic equilibrium is isotope exchange experiments, making a
308 sufficiently long time series of the utmost importance. The shortest experiment in the time series
309 from Elardo and Shahar (2017), lasting 30 minutes at 1850 °C, did achieve equilibrium and had
310 the same $\Delta^{57}Fe_{Metal\text{-}Silicate}$ as longer runs up to 3 hours. The experimental temperatures cannot fully
311 explain the differences in the Poitrasson et al. (2009) results. Adjustment of the $\Delta^{57}Fe_{Metal\text{-}Silicate}$ of
312 0.134 ‰ at 1750 °C to 2000 °C using a $1/T^2$ relationship results in a $\Delta^{57}Fe_{Metal\text{-}Silicate}$ of 0.11 ‰,
313 which is higher than the average of their 2000 °C experiments by more than a factor of two. We
314 conclude that it is likely PC-564b is the only experiment from Poitrasson et al. (2009) that achieved
315 isotopic equilibrium and therefore we have included it in our compositional regression (Fig. 3 and
316 Eqs. 1 and 2).
317 Hin et al. (2012) presented the results of ten experiments designed to investigate
318 fractionation at lower temperature. In order to lower the melting point of their Fe-alloys to below
319 their run conditions of 1250-1300 °C and ~1 GPa, they added ~25 wt. % Sn to their metal starting

materials. Capsules were either graphite, which introduced C into the Fe-Sn-alloys, or SiO_2 glass. Durations were between 0.4 and 16 hours and equilibrium was assessed with a time series. The largest deviation from 0‰ in $\Delta^{56}Fe_{Metal\text{-}Silicate}$ outside of uncertainty observed by Hin et al. (2012) was 0.02‰ in a single experiment at 1250 °C and therefore they argued that core formation would not result in a detectable fractionation of Fe isotopes.

The experiments of Hin et al. (2012) are difficult to interpret for a few reasons. Firstly, the phase relations in the Fe-Sn-C system are poorly known. If we consider the C-free ambient pressure Fe-Sn binary phase diagram (Hansen, 1958), the alloys in their experiments at 1250 – 1300 °C should have been below the liquidus. The added pressure of the experiments should increase the liquidus temperature, so it is likely that the Hin et al. (2012) experiments contained two Fe-Sn phases. Backscattered electron images clearly showed two metallic phases in at least one experiment, although the composition of only one phase is reported. This feature was interpreted to be the result of exsolution upon quench; however, the morphology of the coexisting alloys in their images (fully separated, discrete phases with smooth boundaries; Fig. 1c in Hin et al., 2012) indicate it is more likely to be an equilibrium feature. Together, these observations make it difficult to interpret the compositional relationships of the metallic phases relative to the isotopic compositions. Secondly, the effects of Sn in Fe-alloys on the fractionation of Fe isotopes are difficult to determine. The metallic radii difference between Sn and Fe leaves the former on the very upper edge of the substitutional alloy "favorable zone" defined by Hume-Rothery (1966), which is the range in metallic radii that are favorable to the formation of a substitutional alloy with Fe. However, Sn does not appear to have the same effect on Fe isotopic fractionation that has been demonstrated by our experiments for other substitutional elements (Fig. 3b). One possibility is that Sn affects the structure of the Fe-Sn alloys in a way that differs from Ni, S, and Si. The Fe-Sn

phase diagram shows a complex liquidus topology, including a region of two-liquid immiscibility, indicative of non-ideal mixing between Fe and Sn. Because the effects of Sn on the bonding environment of metals are poorly known, we strongly advise against the use of Sn in future experimental studies of isotope fractionation.

Another possibility for the results in Hin et al. (2012) is incomplete separation of the metal and silicate phases. It is useful to remember that measured fractionation factors in isotope exchange experiments are minimum values, as impure phase separates will artificially produce fractionation factors closer to 0‰ than the true value. Whatever the cause, the results of Hin et al. (2012) are inconsistent with multiple other piston cylinder studies (Shahar et al., 2015; Elardo and Shahar, 2017) and thus we have not included their data in our regressions.

4.5 – Estimates of the Iron Isotope Compositions of Planetary Mantles Using Experiments

Appropriate values of $\Delta^{57}Fe_{Metal\text{-}Silicate}$ to model core formation were calculated using Eq. 2. Estimated ranges of core-mantle equilibration temperatures were 2050 – 3350 K for the Moon, 1900 – 2300 K for Mars, and 1725 – 2000 K for Vesta (Righter and Drake, 1996; Righter and Chabot, 2011; Pringle et al., 2013; Steenstra et al., 2016a; 2016b). Estimated ranges for X_{sub} in at. % in planetary cores were 7.9 – 61.7 for the Moon, 8.0 – 36.4 for Mars, and 7.5 – 28.4 for Vesta (Dreibus and Wänke, 1980; O'Neill, 1991; Righter and Drake, 1996; Mittlefehldt et al., 1998; Weber et al., 2011). We can then calculate a range of $\delta^{57}Fe_{Mantle}$ for each planetary mantle with the isotope mass balance relationship:

$$\delta^{57}Fe_{Bulk\ Planet} = \left(\Delta^{57}Fe_{Metal-Silicate} + \delta^{57}Fe_{Mantle}\right) \times (1 - fFe_{Mantle}) + \delta^{57}Fe_{Mantle} \times fFe_{Mantle} \qquad (Eq. 3)$$

Where $f\mathrm{Fe}_{\mathrm{Mantle}}$ is the mass fraction of Fe in the bulk silicate portion of each planetary body. Ranges for $f\mathrm{Fe}_{\mathrm{Mantle}}$ were calculated using estimates for the core mass fraction and bulk silicate Fe content of 0.024 and 5.51 wt.%, respectively for the Moon, 0.206 and 13.4 wt. % for Mars, and 0.180 and 11.15 wt. % for Vesta (Dreibus and Wänke, 1985; Lodders and Fegley, 1997; Ruzicka et al., 1997; Longhi, 2006; Russell et al., 2012; Steenstra et al., 2016b). We assume that $\delta^{57}\mathrm{Fe}_{\mathrm{Bulk\ Planet}}$ is equal to the chondritic value of ~0‰. Our calculations update those presented by Elardo and Shahar (2017) by incorporating our new experiments in Eqs. 1 and 2. We do not estimate Earth's mantle because it is unlikely our experiments at 1 GPa capture the appropriate bonding environments for Fe at terrestrial core formation conditions. The δ^{57}Fe of the BSE (or at least the sampled upper mantle) is best constrained by the compositions of peridotite xenoliths (Dauphas et al., 2017), which have a strong peak in compositions δ^{57}Fe = -0.039‰, although some mantle heterogeneity and uncertainty regarding the BSE value certainly exists (Poitrasson et al., 2013; Williams and Bizimis, 2014). Our model predicts that the $\delta^{57}\mathrm{Fe}_{\mathrm{Mantle}}$ is between -0.01‰ to -0.12‰ for the Moon, -0.06‰ to -0.33‰ for Mars, and -0.08‰ to -0.33‰ for Vesta. The model predicts a more restricted range for the lunar mantle due to the small size of the lunar core (i.e., a high $f\mathrm{Fe}_{\mathrm{Mantle}}$) and the ranges are a function of the ranges in estimates of core-mantle equilibration temperature and X_{sub} listed above.

4.6 – Estimates of the Iron Isotope Compositions of Planetary Mantles Using Samples

387 *4.6.1 – The Moon*

388 Lunar basalts span a large range in δ^{57}Fe from roughly chondritic compositions in some
389 picritic volcanic glasses to very heavy values in high-Ti basalts (Poitrasson et al., 2004; Weyer et
390 al., 2004), leading some workers to conclude that the heavy average composition of lunar basalts
391 is indicative of a heavy bulk silicate Moon. Although the low-Ti mare basalt suite has been
392 previously used to estimate the δ^{57}Fe of bulk Moon (Poitrasson et al., 2004; Dauphas et al., 2017),
393 they are partial melts of lunar mantle source regions that formed after significant amounts (>80%)
394 of crystal fractionation in the magma ocean as evidenced by ubiquitous negative Eu anomalies.
395 Even small (e.g., <0.1‰) mineral-melt fractionation factors could cause significant Fe isotope
396 fractionation over the course of magma ocean fractional crystallization (e.g., Wang et al., 2015).
397 Thus, it is unlikely that the δ^{57}Fe of low-Ti basalt source regions is similar to that of the bulk
398 silicate Moon. Additionally, samples of the Mg-suite plutonic rocks have been used to estimate
399 the composition of the lunar mantle because they have an Mg# close to that of the bulk Moon
400 (Wang et al., 2015; Sossi and Moynier, 2017). However, the Mg-suite are cumulate rocks, not
401 magmatic liquid compositions, and their parental melts incorporated significant amounts of both
402 crustal anorthosite and the highly geochemically fractionated KREEP reservoir (Papike et al.,
403 1996; Elardo et al., 2011; Shearer et al., 2015), so their positive δ^{57}Fe ranging from 0.05 – 0.10‰
404 (Sossi and Moynier, 2017) is reflective of Fe sourced from multiple geochemical reservoirs, some
405 of which have been highly fractionated, and thus will not be reflective of the δ^{57}Fe of the bulk
406 silicate Moon.

407 In order to estimate the δ^{57}Fe of a primitive lunar mantle source region, Elardo and Shahar
408 (2017) used the δ^{57}Fe of -0.027 ± 0.050‰ of the Apollo 15 green glass from Poitrasson et al.
409 (2004). The Apollo 15 green glasses represent the most primitive mantle melts from the Moon

currently known (Longhi, 1992), so they are the lunar samples most likely to record a mantle $\delta^{57}Fe$ close to the bulk silicate Moon value (also see Supplementary Information in Elardo and Shahar, 2017). Measured compositions of the green glass are somewhat varied (Weyer et al., 2004; Sossi and Moynier, 2017). This could be the result of variability in the five different magma compositions present in the green glass deposit or possibly the accumulation of isotopically light Fe deposited on glass bead surfaces during fire fountaining. The latter has been suggested to have affected the isotopic compositions of more volatile elements such as Zn (Kato et al., 2015); however, given that Fe is significantly less volatile than Zn, that the volcanic glass beads contain ~3 orders of magnitude more Fe than Zn, and that glass bead coatings are volumetrically very small compared to the beads themselves, it remains to be demonstrated that Fe in bead coatings has an effect on the measured $\delta^{57}Fe$ of the glasses. Therefore, using the composition of the Apollo 15 green glass and the $\Delta^{57}Fe_{Mantle\text{-}Melt}$ of -0.07‰ estimated by Elardo and Shahar (2017) for melting of reduced mantles (see the Supplementary Information in that study for rationale for this fractionation factor), the $\delta^{57}Fe$ of the green glass source region would be -0.10 ± 0.05‰. We consider this value to be best sample-based estimate available for a primitive lunar mantle source region and is perhaps close to that of the bulk silicate Moon. This mantle value agrees well with the range predicted by our model (Fig. 5).

4.6.2 – Mars

There is no obvious single basaltic shergottite that could be used to estimate the $\delta^{57}Fe$ of the primitive martian mantle. Sossi et al. (2016a) corrected the measured $\delta^{57}Fe$ of a suite of martian samples to account for accumulation of olivine and pyroxene (assuming a $\Delta^{57}Fe_{Mineral\text{-}Melt}$ of -0.10‰) to calculate parental melt compositions and subsequently the $\delta^{57}Fe$ at the Mg# estimated

for the bulk martian mantle. Their estimate of the $\delta^{57}Fe$ of the martian mantle is -0.04 ± 0.03‰. Although Sossi et al. (2016a) provided the best estimates for the $\delta^{57}Fe$ values of magmas parental to the martian meteorites available, they did not take into account fractionation during mantle partial melting. Experimentally determined liquidus multiple saturation points for martian basalts indicate they are derived from mantle source regions consisting of olivine and low-Ca pyroxene (e.g., Musselwhite et al., 2006), so by definition that -0.10‰ fractionation must apply during mantle melting as well, as both fractionation during melting and subsequent fractional crystallization in the melt should have similar effects when the same phases are present. If we take the lightest (i.e., most primitive) $\delta^{57}Fe$ for a martian parental liquid (LAR 06319) calculated by Sossi et al. (2016a) and apply a $\Delta^{57}Fe_{Mantle\text{-}Melt}$ of -0.10‰, we calculate a $\delta^{57}Fe$ of -0.12 ± 0.04‰ for its mantle source region, within the range predicted by our model (Fig. 5). Clearly there is heterogeneity in the martian mantle, given the scatter in Mg# vs. $\delta^{57}Fe$ for martian parental liquids (Sossi et al., 2016a), which could be attributed to magma ocean crystallization, mantle mixing during convection, and/or previous episodes of melt extraction. However, we consider -0.12‰ to be a reasonable estimate for the $\delta^{57}Fe$ of a primitive martian mantle source region.

4.6.3 – Vesta

The $\delta^{57}Fe$ values of non-cumulate eucrites likely have a different relationship to the $\delta^{57}Fe$ of the bulk vestian mantle than do basaltic samples from Earth, the Moon, and Mars. Eucrites have been proposed to represent partial melts of an undifferentiated, chondritic mantle (Stolper, 1977) or residual liquids from crystallization of a magma ocean (Righter and Drake, 1997; Ruzicka et al., 1997). However, each of these models have difficulty explaining the bulk compositions of eucrites, their limited compositional range, and/or their relationships to diogenites (Mandler and

456 Elkins-Tanton, 2013). A variation of the magma ocean residual liquid model proposed by Mandler
457 and Elkins-Tanton (2013) showed that 60 – 70% equilibrium crystallization of a vestian magma
458 ocean followed by extraction of the residual liquid to shallow magma chambers that are
459 periodically recharged can explain the narrow compositional range in the eucrites while
460 simultaneously producing diogenite cumulates. This model may also account for why the eucrites
461 exhibit a narrow range in δ^{57}Fe. Both equilibrium crystallization of the vestian magma ocean and
462 replenishment of eucrite magma chambers would limit the range in δ^{57}Fe compared with that
463 produced by fractional crystallization.

464 In all models of eucrite petrogenesis from a magma ocean, the non-cumulate eucrites with
465 the lightest δ^{57}Fe would be the most primitive, as fractionation during crystallization of the residual
466 melts would enrich the melt in heavy isotopes (Weyer and Ionov, 2007; Craddock et al., 2013;
467 Teng et al., 2013; Dauphas et al., 2014). Therefore, we use the δ^{57}Fe of -0.035 ± 0.042‰ the eucrite
468 Juvinas (Poitrasson et al., 2004), the lightest δ^{57}Fe measured for a non-cumulate eucrite, and the
469 $\Delta^{57}Fe_{Mantle\text{-}Melt}$ of -0.07‰ estimated by Elardo and Shahar (2017) to estimate the δ^{57}Fe of a
470 primitive mantle source region in Vesta to be -0.11 ± 0.04‰. This primitive mantle source region
471 composition agrees well with the mantle range predicted by our core formation model (Fig. 5).
472
473 **4.7 – Are Volatile Depletion Processes Recorded by Iron Isotopes?**
474 Fractionations of Fe isotopes relative to chondrites in various planetary sample suites have
475 been attributed by some workers to volatile depletion processes. Poitrasson et al. (2004) suggested
476 that the Moon-forming giant impact may have fractionated Fe isotopes, leaving the residual silicate
477 Moon and Earth heavy. Sossi et al. (2016a) suggested that fractionation during volatile loss events
478 was more widespread and occurred in either the nebular or post-nebular phase of accretion based

479 on an apparent correlation between Fe/Mn and δ^{57}Fe in basalts from Earth, the Moon, Mars, and
480 Vesta, and in ureilites and angrites. However, neither model accounted for Fe isotope fractionation
481 during core formation. Additionally, the apparent correlation between Fe/Mn and δ^{57}Fe is
482 predicated, in part, on a heavy isotopic composition for Earth, which is still heavily debated (see
483 Dauphas et al., 2017), and also implies that Vesta is one of the least volatile depleted differentiated
484 bodies despite geochemical evidence that it is one of the most depleted (e.g., Mittlefehldt, 1987),
485 which suggest that the correlation may be an artifact arising from the assumed bulk δ^{57}Fe of each
486 body.

487 In Fig. 6a we compare the Fe/Mn of Earth, the Moon, Mars, and Vesta (O'Neill and Palme,
488 2008) to peak δ^{57}Fe value of terrestrial peridotites and the calculated δ^{57}Fe of the mantle source
489 regions of the Apollo 15 green glasses, basaltic shergottite LAR 06316, and the Juvinas eucrite.
490 We do not consider the ureilites or angrites here because these meteorites groups have very
491 complex mineralogy, geochemistry, and petrogenetic histories (e.g., Mittlefehldt et al., 1998) that
492 do not make their δ^{57}Fe easily relatable to the bulk δ^{57}Fe of their parent bodies. Figure 6a shows
493 that there is no correlation between the δ^{57}Fe of primitive mantle source regions and Fe/Mn that
494 would be indicative of Fe isotope fractionation by volatile depletion. The δ^{57}Fe and Fe/Mn of
495 planetary mantles can be explained by a combination of isotope fractionation during core
496 formation and elemental volatile depletion processes that do not affect Fe isotopes (Fig. 6a). Some
497 Fe isotope fractionation via volatile depletion cannot be completely ruled out, as these processes
498 are not mutually exclusive, and in a δ^{57}Fe vs. Fe/Mn plot these processes would qualitatively drive
499 planetary mantles in different directions, making the deconvolution of their relative effects
500 difficult.

501 Therefore, to further assess the possibility of Fe isotope fractionation during volatile depletion,
502 we consider three elemental ratios that are diagnostic of volatile depletion (Halliday and Porcelli,
503 2001; O'Neill and Palme, 2008) but are not affected by core formation: Mn/Na, Rb/Sr, and K/U.
504 Figure 6b-d shows that there are no discernible correlations between the δ^{57}Fe of planetary mantles
505 and these ratios. In all cases, the δ^{57}Fe of planetary mantles can be explained by a combination of
506 the core formation process fractionating Fe isotopes and volatile depletion processes affecting the
507 elemental Mn/Na, Rb/Sr, and K/U without noticeably fractionating Fe isotopes.
508
509 **4.8 – Fe Isotope Evolution During Planetary Differentiation**
510 Our schematic model for how Fe isotopes fractionate during accretion, differentiation, and
511 mantle melting is shown in Fig. 7. The solar nebula was likely homogeneous in terms of Fe
512 isotopes, as indicated by chondrites (e.g., Craddock and Dauphas, 2011). We do not find robust
513 evidence of fractionation via volatilization during planetary accretion (e.g., Fig. 6), though its
514 effects may have been overprinted by other processes. Experiments show that fractionation during
515 core formation results in light mantles and heavy cores in the smaller planets and asteroids (Fig.
516 3). The higher temperatures during Earth's core formation and the effects of pressure on the
517 bonding environment of Fe appear to have resulted in little to no fractionation in Earth's mantle,
518 as evidenced by the global peridotite suite (e.g., Craddock et al., 2013; Dauphas et al., 2017). The
519 Fe isotope difference between abyssal peridotites and MORBs, and the very wide range in δ^{57}Fe
520 in lunar basalts demonstrate that mineral-melt equilibrium enriches the melt in heavy isotopes.
521 Fractional crystallization of the lunar magma ocean likely created a heterogeneous mantle and
522 further fractionation during subsequent mantle partial melting produced the range observed in
523 lunar basalts. The more restricted range in shergottites and basaltic eucrites may be the result of

non-representative sampling from those bodies, re-homogenization during mantle convection on Mars, and/or more restricted fractionation during equilibrium crystallization of the vestian magma ocean.

ACKNOWLEDGEMENTS

We are grateful to Mary F. Horan for her assistance in the Carnegie DTM chemistry lab. We thank Nancy Chabot and Franck Poitrasson for thorough and thoughtful reviews and Fred Moynier for his editorial handling. This work was funded by NSF grant EAR-1321858 to A. S. This work was performed under the auspices of the U.S. Department of Energy by Lawrence Livermore National Laboratory under Contract DE-AC52-07NA27344. This is release number LLNL-JRNL-753799.

REFERENCES

Bourdon, B., Roskosz, M., Hin, R.C., 2018. Isotope tracers of core formation. Earth-Sci Rev 181, 61-81.

Cao, X., Bao, H., 2017. Redefining the utility of the three-isotope method. Geochim Cosmochim Ac 212, 16-32.

Craddock, P.R., Dauphas, N., 2011. Iron Isotopic Compositions of Geological Reference Materials and Chondrites. Geostandards and Geoanalytical Research 35, 101-123.

Craddock, P.R., Warren, J.M., Dauphas, N., 2013. Abyssal peridotites reveal the near-chondritic Fe isotopic composition of the Earth. Earth and Planetary Science Letters 365, 63-76.

545 Dauphas, N., John, S.G., Rouxel, O., 2017. Iron Isotope Systematics, in: Teng, F.Z., Dauphas, N.,
546 Watkins, J.M. (Eds.), Non-Traditional Stable Isotopes. Reviews in Mineralogy and
547 Geochemistry Vol. 82, Ch. 11, Minerological Society of America, pp. 415-510.
548 Dauphas, N., Roskosz, M., Alp, E.E., Neuville, D.R., Hu, M.Y., Sio, C.K., Tissot, F.L.H., Zhao,
549 J., Tissandiere, L., Medard, E., Cordier, C., 2014. Magma redox and structural controls on iron
550 isotope variations in Earth's mantle and crust. Earth and Planetary Science Letters 398, 127-
551 140.
552 Dreibus, G., Wänke, H., 1980. The Bulk Composition of the Eucrite Parent Asteroid and Its
553 Bearing on Planetary Evolution. Zeitschrift Fur Naturforschung Section a-a Journal of Physical
554 Sciences 35, 204-216.
555 Dreibus, G., Wänke, H., 1985. Mars, a volatile-rich planet. Hans Suess Festschrift 20, 367-381.
556 Elardo, S.M., Draper, D.S., Shearer, C.K., 2011. Lunar Magma Ocean crystallization revisited:
557 Bulk composition, early cumulate mineralogy, and the source regions of the highlands Mg-
558 suite. Geochim Cosmochim Ac 75, 3024-3045.
559 Elardo, S.M., Shahar, A., 2017. Non-chondritic iron isotope ratios in planetary mantles as a result
560 of core formation. Nat Geosci 10, 317-321.
561 Halliday, A.N., Porcelli, D., 2001. In search of lost planets - the paleocosmochemistry of the inner
562 solar system. Earth and Planetary Science Letters 192, 545-559.
563 Hansen, M. 1958. Constitution of binary alloys, 2nd ed. Prepared with the cooperation of Kurt
564 Anderko. ed., McGraw Hill.
565 Hin, R.C., Schmidt, M.W., Bourdon, B., 2012. Experimental evidence for the absence of iron
566 isotope fractionation between metal and silicate liquids at 1 GPa and 1250-1300 °C and its
567 cosmochemical consequences. Geochim Cosmochim Ac 93, 164-181.

568 Hume-Rothery, W., 1966. The structures of alloys of iron: an elementary introduction. Permagon
569 Press.
570 Jordan, M.K., Tang, H.L., Kohl, I.E., Young, E.D., 2019. Iron isotope constraints on planetesimal
571 core formation in the early solar system. Geochim Cosmochim Ac 246, 461-477.
572 Kato, C., Moynier, F., Valdes, M.C., Dhaliwal, J.K., Day, J.M.D., 2015. Extensive volatile loss
573 during formation and differentiation of the Moon. Nat Commun 6.
574 Kono, Y., Kenney-Benson, C., Shibazaki, Y., Park, C., Shen, G.Y., Wang, Y.B., 2015. High-
575 pressure viscosity of liquid Fe and FeS revisited by falling sphere viscometry using ultrafast
576 X-ray imaging. Phys Earth Planet In 241, 57-64.
577 Liu, J., Dauphas, N., Roskosz, M., Hu, M.Y., Yang, H., Bi, W.L., Zhao, J.Y., Alp, E.E., Hu, J.Y.,
578 Lin, J.F., 2017. Iron isotopic fractionation between silicate mantle and metallic core at high
579 pressure. Nat Commun 8, 14337.
580 Lodders, K., Fegley, B., 1997. An oxygen isotope model for the composition of Mars. Icarus 126,
581 373-394.
582 Longhi, J., 1992. Experimental petrology and petrogenesis of mare volcanics. Geochim
583 Cosmochim Ac 56, 2235-2251.
584 Longhi, J., 2006. Petrogenesis of picritic mare magmas: Constraints on the extent of early lunar
585 differentation. Geochim Cosmochim Ac 70, 5919-5934.
586 Mandler, B.E., Elkins-Tanton, L.T., 2013. The origin of eucrites, diogenites, and olivine
587 diogenites: Magma ocean crystallization and shallow magma chamber processes on Vesta.
588 Meteorit Planet Sci 48, 2333-2349.
589 Mittlefehldt, D.W., 1987. Volatile Degassing of Basaltic Achondrite Parent Bodies: Evidence from
590 Alkali Elements and Phosphorus. Geochim Cosmochim Ac 51, 267-278.

591 Mittlefehldt, D.W., McCoy, T.J., Goodrich, C.A., Kracher, A., 1998. Non-chondritic meteorites
592 from asteroidal bodies. Reviews in Mineralogy Vol 36, Ch. 4, 4-1 – 4-195, Mineralogical
593 Society of America.
594 Musselwhite, D.S., Dalton, H.A., Kiefer, W., Treiman, A.H., 2006. Experimental petrology of the
595 basaltic shergottite Yamato-980459: Implications for the thermal structure of the Martian
596 mantle. Meteoritics and Planetary Science 41, 1271-1290.
597 O'Neill, H.S.C., 1991. The origin of the Moon and the early history of the Earth - a chemical model.
598 Part 1: The Moon. Geochim Cosmochim Ac 55, 1135-1157.
599 O'Neill, H.S.C., Palme, H., 2008. Collisional erosion and the non-chondritic composition of the
600 terrestrial planets. Philosophical Transactions of the Royal Society a-Mathematical Physical
601 and Engineering Sciences 366, 4205-4238.
602 Papike, J.J., Fowler, G.W., Shearer, C.K., Layne, G.D., 1996. Ion microprobe investigation of
603 plagioclase and orthopyroxene from lunar Mg-suite norites: implications for calculating
604 parental melt REE concentrations and for assessing postcrystallization REE redistribution.
605 Geochim Cosmochim Ac 60, 3967-3978.
606 Poitrasson, F., 2007. Does planetary differentiation really fractionate iron isotopes? Earth and
607 Planetary Science Letters 256, 484-492.
608 Poitrasson, F., Delpech, G., Gregoire, M., 2013. On the iron isotope heterogeneity of lithospheric
609 mantle xenoliths: implications for mantle metasomatism, the origin of basalts and the iron
610 isotope composition of the Earth. Contributions to Mineralogy and Petrology 165, 1243-1258.
611 Poitrasson, F., Halliday, A.N., Lee, D.C., Levasseur, S., Teutsch, N., 2004. Iron isotope differences
612 between Earth, Moon, Mars and Vesta as possible records of contrasted accretion mechanisms.
613 Earth and Planetary Science Letters 223, 253-266.

614 Poitrasson, F., Levasseur, S., Teutsch, N., 2005. Significance of iron isotope mineral fractionation
615 in pallasites and iron meteorites for the core-mantle differentiation of terrestrial planets. Earth
616 and Planetary Science Letters 234, 151-164.
617 Poitrasson, F., Roskosz, M., Corgne, A., 2009. No iron isotope fractionation between molten alloys
618 and silicate melt to 2000 degrees C and 7.7 GPa: Experimental evidence and implications for
619 planetary differentiation and accretion. Earth and Planetary Science Letters 278, 376-385.
620 Pringle, E.A., Savage, P.S., Badro, J., Barrat, J.A., Moynier, F., 2013. Redox state during core
621 formation on asteroid 4-Vesta. Earth and Planetary Science Letters 373, 75-82.
622 Righter, K., Chabot, N.L., 2011. Moderately and slightly siderophile element constraints on the
623 depth and extent of melting in early Mars. Meteoritics & Planetary Science 46, 157-176.
624 Righter, K., Drake, M.J., 1996. Core formation in Earth's Moon, Mars, and Vesta. Icarus 124, 513-
625 529.
626 Righter, K., Drake, M.J., 1997. A magma ocean on Vesta: core formation and petrogenesis of
627 eucrites and diogenites. Meteoritics and Planetary Science 32, 929-944.
628 Russell, C.T., Raymond, C.A., Coradini, A., McSween, H.Y., Zuber, M.T., Nathues, A., De
629 Sanctis, M.C., Jaumann, R., Konopliv, A.S., Preusker, F., Asmar, S.W., Park, R.S., Gaskell,
630 R., Keller, H.U., Mottola, S., Roatsch, T., Scully, J.E.C., Smith, D.E., Tricarico, P., Toplis,
631 M.J., Christensen, U.R., Feldman, W.C., Lawrence, D.J., McCoy, T.J., Prettyman, T.H.,
632 Reedy, R.C., Sykes, M.E., Titus, T.N., 2012. Dawn at Vesta: Testing the Protoplanetary
633 Paradigm. Science 336, 684-686.
634 Ruzicka, A., Snyder, G.A., Taylor, L.A., 1997. Vesta as the howardite, eucrite and diogenite parent
635 body: Implications for the size of a core and for large-scale differentiation. Meteoritics &
636 Planetary Science 32, 825-840.

637 Sanloup, C., Fiquet, G., Gregoryanz, E., Morard, G., Mezouar, M., 2004. Effect of Si on liquid Fe
638 compressibility: Implications for sound velocity in core materials. Geophys Res Lett 31.
639 Sanloup, C., Guyot, F., Gillet, P., Fei, Y., 2002. Physical properties of liquid Fe alloys at high
640 pressure and their bearings on the nature of metallic planetary cores. J Geophys Res-Sol Ea
641 107.
642 Sanloup, C., Guyot, F., Gillet, P., Fiquet, G., Hemley, R.J., Mezouar, M., Martinez, I., 2000.
643 Structural changes in liquid Fe at high pressures and high temperatures from synchrotron X-
644 ray diffraction. Europhys Lett 52, 151-157.
645 Schenk, T., Holland-Moritz, D., Simonet, V., Bellissent, R., Herlach, D.M., 2002. Icosahedral
646 short-range order in deeply undercooled metallic melts. Phys Rev Lett 89.
647 Schoenberg, R., von Blanckenburg, F., 2006. Modes of planetary-scale Fe isotope fractionation.
648 Earth and Planetary Science Letters 252, 342-359.
649 Shahar, A., Elardo, S.M., Macris, C.A., 2017. Equilibrium Fractionation of Non-traditional Stable
650 Isotopes: an Experimental Perspective. Rev Mineral Geochem Vol. 82, Ch. 3, 65-83,
651 Minerlaogical Society of America.
652 Shahar, A., Hillgren, V.J., Horan, M.F., Mesa-Garcia, J., Kaufman, L.A., Mock, T.D., 2015.
653 Sulfur-controlled iron isotope fractionation experiments of core formation in planetary bodies.
654 Geochim Cosmochim Ac 150, 253-264.
655 Shahar, A., Schauble, E.A., Caracas, R., Gleason, A.E., Reagan, M.M., Xiao, Y., Shu, J., Mao,
656 W., 2016. Pressure-dependent isotopic composition of iron alloys. Science 352, 580-582.
657 Shahar, A., Young, E.D., Manning, C.E., 2008. Equilibrium high-temperature Fe isotope
658 fractionation between fayalite and magnetite: An experimental calibration. Earth and Planetary
659 Science Letters 268, 330-338.

660 Shearer, C.K., Elardo, S.M., Petro, N.E., Borg, L.E., McCubbin, F.M., 2015. Origin of the lunar
661 highlands Mg-suite: An integrated petrology, geochemistry, chronology, and remote sensing
662 perspective. American Mineralogist 100, 294-325.
663 Shibazaki, Y., Kono, Y., Fei, Y.W., 2015. Microscopic structural change in a liquid Fe-C alloy of
664 similar to 5GPa. Geophys Res Lett 42, 5236-5242.
665 Sossi, P.A., 2017. A nickel for your planet's thoughts. Nat Geosci 10, 249-251.
666 Sossi, P.A., Moynier, F., 2017. Chemical and isotopic kinship of iron in the Earth and Moon
667 deduced from the lunar Mg-Suite. Earth Planet Sc Lett 471, 125-135.
668 Sossi, P.A., Nebel, O., Anand, M., Poitrasson, F., 2016a. On the iron isotope composition of Mars
669 and volatile depletion in the terrestrial planets. Earth and Planetary Science Letters 449, 360-
670 371.
671 Sossi, P.A., Nebel, O., Foden, J., 2016b. Iron isotope systematics in planetary reservoirs. Earth
672 Planet Sc Lett 452, 295-308.
673 Steenstra, E.S., Knibbe, J.S., Rai, N., van Westrenen, W., 2016a. Constraints on core formation in
674 Vesta from metal-silicate partitioning of siderophile elements. Geochim Cosmochim Ac 177,
675 48-61.
676 Steenstra, E.S., Rai, N., Knibbe, J.S., Lin, Y.H., van Westrenen, W., 2016b. New geochemical
677 models of core formation in the Moon from metal-silicate partitioning of 15 siderophile
678 elements. Earth and Planetary Science Letters 441, 1-9.
679 Stolper, E., 1977. Experimental petrology of eucritic meteorites. Geochim Cosmochim Ac 41, 587-
680 611.
681 Teng, F.Z., Dauphas, N., Huang, S.C., Marty, B., 2013. Iron isotopic systematics of oceanic
682 basalts. Geochim Cosmochim Ac 107, 12-26.

683 Wang, K., Jacobsen, S.B., Sedaghatpour, F., Chen, H., Korotev, R.L., 2015. The earliest Lunar
684 Magma Ocean differentiation recorded in Fe isotopes. Earth and Planetary Science Letters 430,
685 202-208.
686 Wang, K., Moynier, F., Dauphas, N., Barrat, J.A., Craddock, P., Sio, C.K.I., 2012. Iron isotope
687 fractionation in planetary crusts. Geochim Cosmochim Ac 89, 31-45.
688 Weber, R.C., Lin, P.-Y., Garnero, E.J., Williams, Q., Lognonne, P., 2011. Seismic Detection of
689 the Lunar Core. Science 331, 309-312.
690 Weyer, S., Anbar, A.D., Brey, G.P., Munker, C., Mezger, K., Woodland, A.B., 2005. Iron isotope
691 fractionation during planetary differentiation. Earth and Planetary Science Letters 240, 251-
692 264.
693 Weyer, S., Ionov, D.A., 2007. Partial melting and melt percolation in the mantle: The message
694 from Fe isotopes. Earth and Planetary Science Letters 259, 119-133.
695 Weyer, S., Woodland, A., Munker, C., Arnold, G.L., Chakrabarti, R., Anbar, A.D., 2004. Iron
696 isotope variations in the Earth's mantle and the terrestrial planets. Geochim Cosmochim Ac
697 68, A736-A736.
698 Williams, H.M., Bizimis, M., 2014. Iron isotope tracing of mantle heterogeneity within the source
699 regions of oceanic basalts. Earth and Planetary Science Letters 404, 396-407.
700 Williams, H.M., Markowski, A., Quitte, G., Halliday, A.N., Teutsch, N., Levasseur, S., 2006. Fe
701 isotope fractionation in iron meteorites: New insights into metal-sulphide segregation and
702 planetary accretion. Earth and Planetary Science Letters 250, 486-500.
703 Williams, H.M., Peslier, A.H., McCammon, C., Halliday, A.N., Levasseur, S., Teutsch, N., Burg,
704 J.P., 2005. Systematic iron isotope variations in mantle rocks and minerals: The effects of
705 partial melting and oxygen fugacity. Earth and Planetary Science Letters 235, 435-452.

706 Williams, H.M., Wood, B.J., Wade, J., Frost, D.J., Tuff, J., 2012. Isotopic evidence for internal
707 oxidation of the Earth's mantle during accretion. Earth and Planetary Science Letters 321, 54-
708 63.
709 Young, E.D., Manning, C.E., Schauble, E.A., Shahar, A., Macris, C.A., Lazar, C., Jordan, M.,
710 2015. High-temperature equilibrium isotope fractionation of non-traditional stable isotopes:
711 Experiments, theory, and applications. Chemical Geology 395, 176-195.
712 Zhao, X.M., Zhang, H.F., Zhu, X.K., Tang, S.H., Tang, Y.J., 2010. Iron isotope variations in spinel
713 peridotite xenoliths from North China Craton: implications for mantle metasomatism.
714 Contributions to Mineralogy and Petrology 160, 1-14.
715
716
717 **FIGURE CAPTIONS**
718 **Figure 1:** Backscattered electron (BSE) images of two experiments from this study. Black regions
719 are epoxy or graphite from the sample capsule. Gray regions are quenched melt and the bright
720 regions are Si-C-Fe alloy. The patchy discoloration on the surface of some of the alloys is oxidation
721 from polishing and black inclusions in the alloys are graphite from the sample capsule.
722
723 **Figure 2:** Metal – silicate fractionation factors at 1850 °C and 1 GPa for Fe isotope exchange
724 experiments vs. the amount of Si in at. % in the Fe-alloy. Uncertainties are 2 standard errors.
725
726 **Figure 3:** Metal – silicate fractionation factors at 1850 °C and 1 GPa for Fe isotope exchange
727 experiments as a function of the total amount of non-Fe elements in the Fe-alloy (a) and the total
728 amount of non-Fe elements that substitute for Fe atoms in the Fe-alloy structure (i.e., Ni, S, Si)

729 (b). Solid and dashed lines are least-squares linear regressions and 95% confidence envelopes,
730 respectively. The Fe-C data are not included in the regression in (b) (see section 4.3). The Fe-Si-
731 C data are from this work. The Fe-Ni-S-N experiments are from Shahar et al. (2015) corrected to
732 1850 °C using the $1/T^2$ relationship. The Fe-C and Fe-Ni-C experiments are from Elardo and
733 Shahar (2017). The single Fe-Ni-C-S experiment is PC-564b from Poitrasson et al. (2009)
734 corrected to 1850 °C. Uncertainties are 2 standard errors.
735
736 **Figure 4:** A plot of nearest neighbor distances in Å for Fe atoms in molten Fe and Fe-alloys as a
737 function of the total amount of non-Fe elements in each alloy. Solid and dashed lines are a least-
738 squares linear regression and 95% confidence envelope, respectively. Data for molten Fe are from
739 Sanloup et al. (2000) and Kono et al. (2015). Data for molten Fe-C alloys is from Shibazaki et al.
740 (2015). Data for molten Fe-Si and Fe-S alloys are from Sanloup et al. (2002). For comparison,
741 pure molten Ni has an r_1 of ~2.49 – 2.48 Å (Schenk et al., 2002).
742
743 **Figure 5:** A plot of estimates of the δ^{57}Fe of the bulk silicate portions of Earth, the Moon, Mars,
744 and Vesta. Shaded bars represent the ranges derived from our experimental model of fractionation
745 during core formation. Data points for the Moon, Mars, and Vesta are estimates of primitive mantle
746 source regions derived from the δ^{57}Fe values basaltic samples (see section 4.6). Data point for
747 Earth's mantle is the composition of the peak in the global peridotite dataset from Dauphas et al.
748 (2017 and references therein). Gray bar is the 95% confidence interval for the average composition
749 of all chondritic meteorites from Craddock and Dauphas (2011).
750

751 **Figure 6:** Plots of the $\delta^{57}Fe$ of primitive mantle sources regions for the Moon, Mars, and Vesta
752 calculated from basalt data (see section 4.6) and the peak in the global peridotite dataset from
753 Dauphas et al. (2017 and references therein) vs. bulk silicate ratios for various indices of volatile
754 depletion, Fe/Mn (a), Mn/Na (b), Rb/Sr (c), and K/U (d). The volatile element ratio data for the
755 chondrite data points are for CI chondrites, whereas the $\delta^{57}Fe$ is the average for all chondrite
756 groups. Ratios are from O'Neill and Palme (2008) and Halliday and Porcelli (2001). Arrows
757 schematically indicate the directions that the processes of core formation, volatile depletion (V.
758 D.) with Fe isotope fractionation, and volatile depletion without Fe isotope fractionation would
759 move planetary mantles relative to chondrites.
760
761 **Figure 7:** A schematic model for the fractionation of Fe isotopes during planetary accretion,
762 differentiation, and mantle melting (figure adapted from Sossi, 2017 based on the model presented
763 by Elardo and Shahar, 2017). Planets and asteroids accrete from a nebula with the observed
764 homogeneous Fe isotope composition of chondrites. Based on the lack of clear correlations
765 between estimates of bulk planetary $\delta^{57}Fe$ and elemental indicators of volatile depletion processes
766 (Fig. 6), we infer no fractionation during accretion. Core formation fractionates Fe isotopes,
767 resulting in heavy cores and isotopically light mantles, at least at relatively low pressure. Mineral-
768 melt fractionation during magma ocean crystallization will result in heterogeneous mantles,
769 especially in regimes where fractional crystallization dominates (e.g., the Moon). Mineral-melt
770 fractionation will also occur during mantle partial melting, as is observed in abyssal peridotite and
771 MORB samples and inferred for other planets. Melts are heavier than their mantle source regions
772 to varying degrees based on redox state, degree of partial melting, and possibly other factors such
773 as source mineralogy. Melting of isotopically light and possibly heterogeneous mantles in the

774 Moon, Mars and Vesta gives rise to the observed range in basaltic compositions from those parent
775 bodies.
776

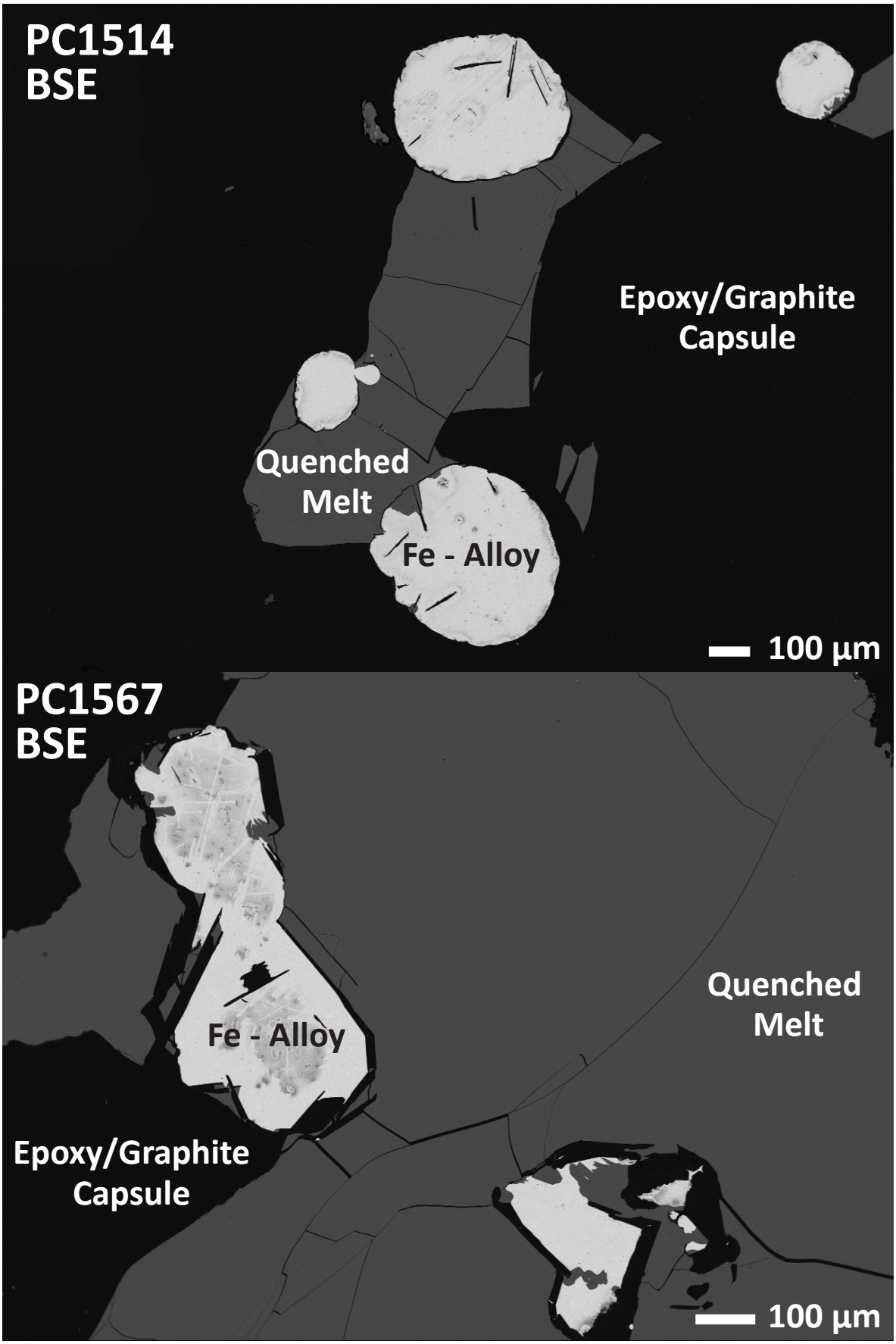
PC1514
BSE
Epoxy/Graphite
Capsule
Quenched
Melt
Fe - Alloy
100 µm
PC1567
BSE
Quenched
Melt
Fe - Alloy
Epoxy/Graphite
Capsule
100 µm

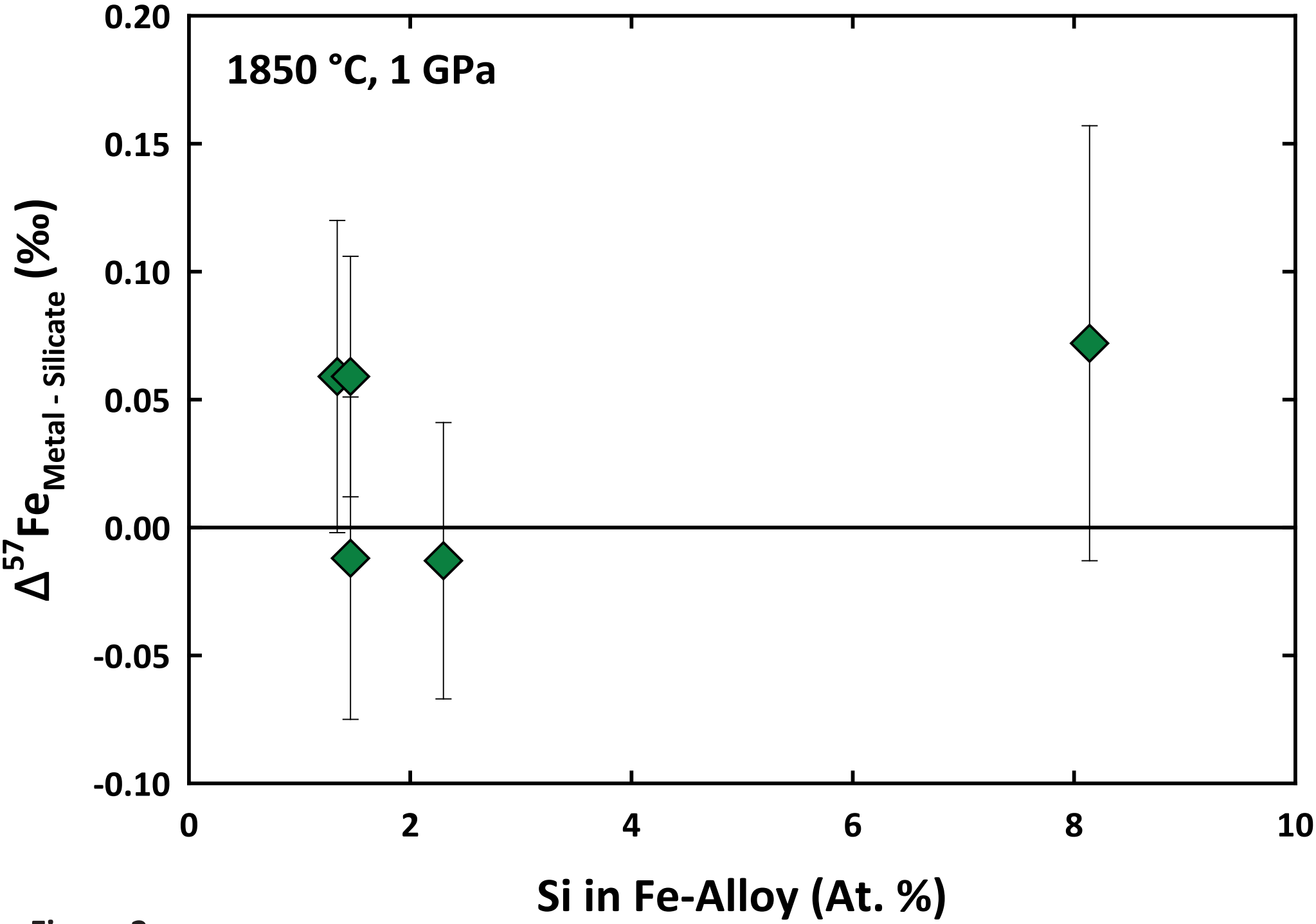
1850 °C, 1 GPa
0.20
0.15
0.10
0.05
0.00
-0.05
-0.10
0
2
4
6
8
10
$\Delta^{57}Fe_{Metal - Silicate}$ (‰)
Si in Fe-Alloy (At. %)

Figure 2

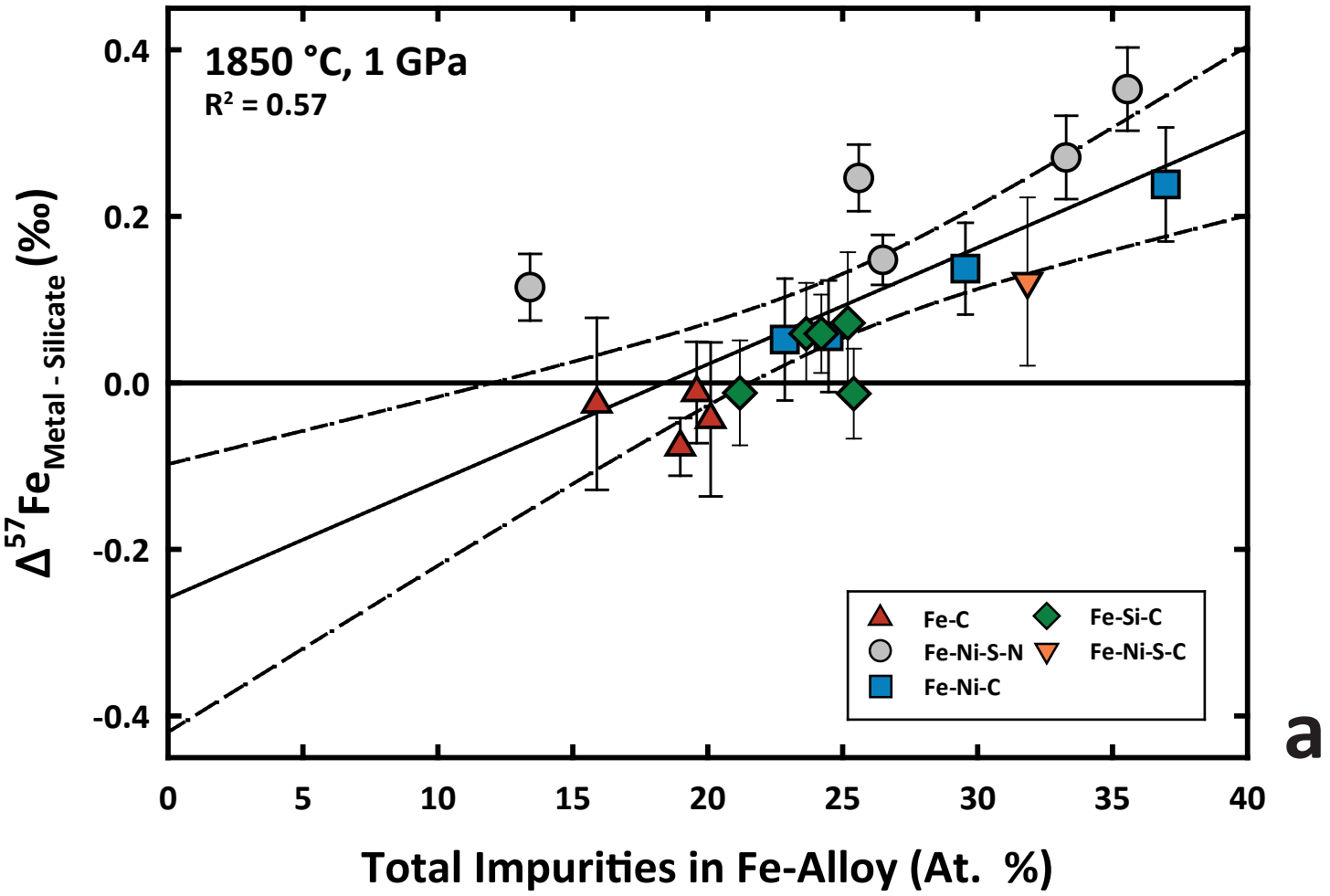
1850 °C, 1 GPa
R² = 0.57
Δ57FeMetal - Silicate (‰)
0.4
0.2
0.0
-0.2
-0.4
0
5
10
15
20
25
30
35
40
Fe-C
Fe-Si-C
Fe-Ni-S-N
Fe-Ni-S-C
Fe-Ni-C
a
Total Impurities in Fe-Alloy (At. %)

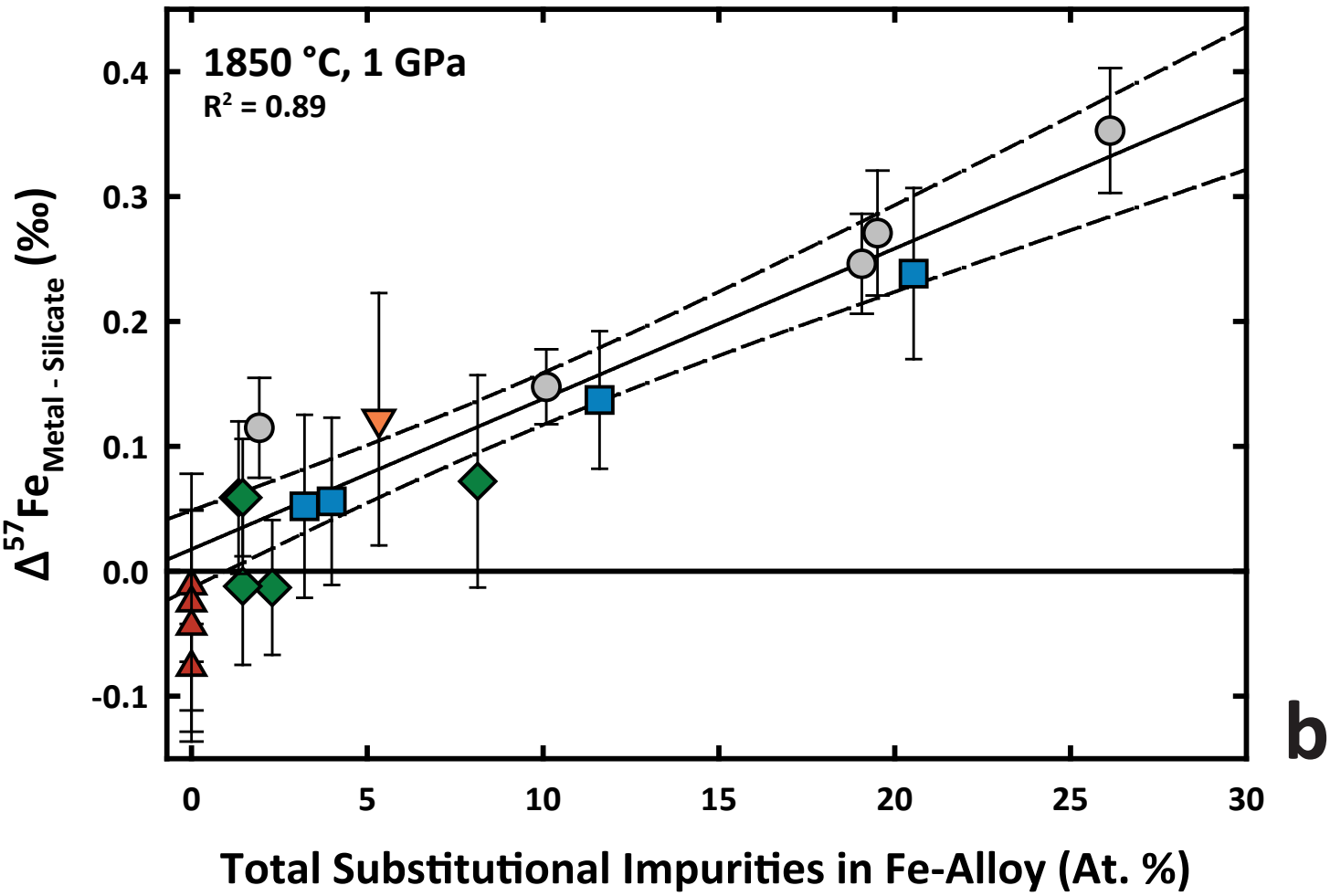
1850 °C, 1 GPa
R² = 0.89
Δ57FeMetal - Silicate (‰)
0.4
0.3
0.2
0.1
0.0
-0.1
0
5
10
15
20
25
30
b
Total Substitutional Impurities in Fe-Alloy (At. %)

Figure 3

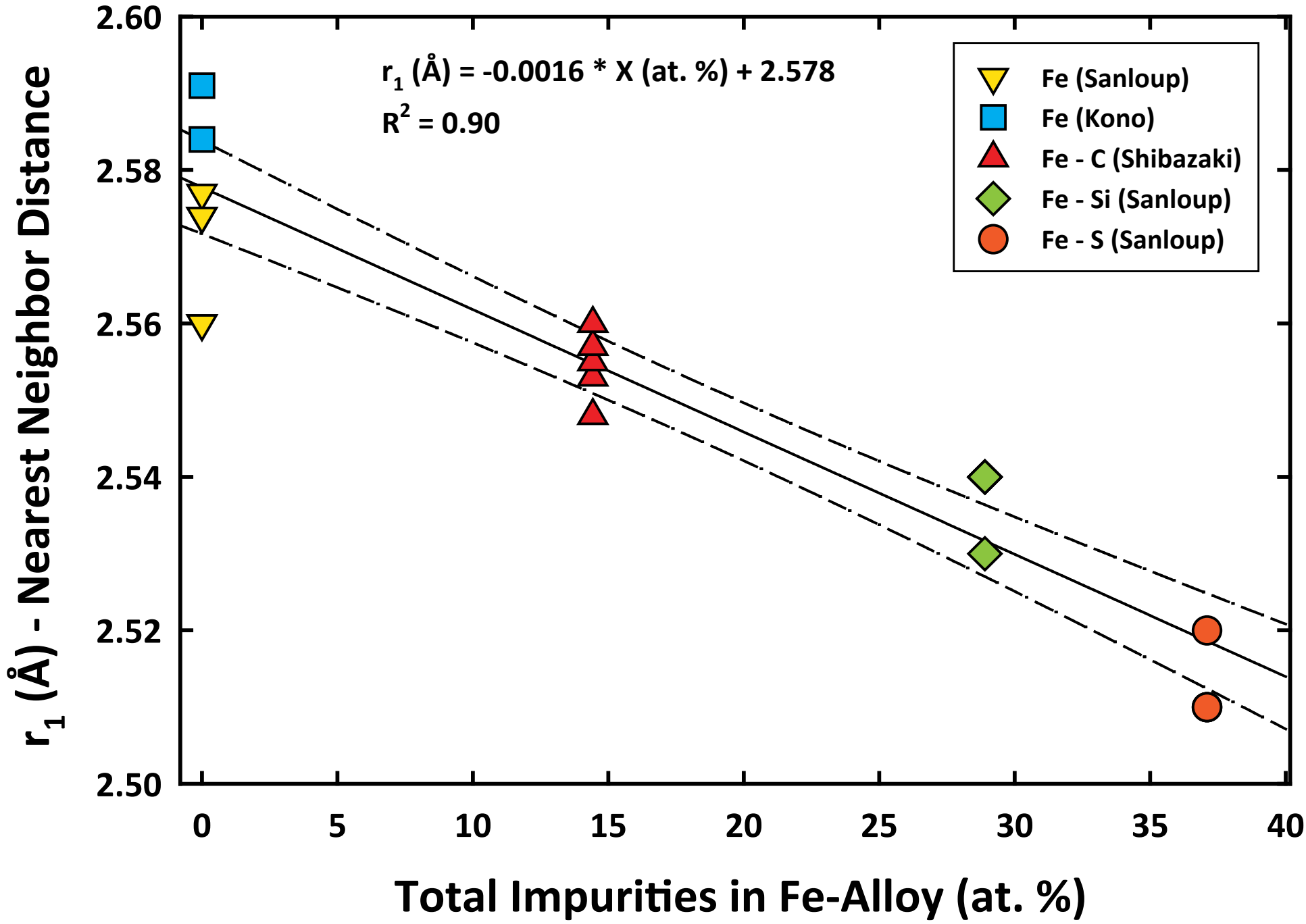
r_1 (Å) = -0.0016 * X (at. %) + 2.578
R^2 = 0.90
Fe (Sanloup)
Fe (Kono)
Fe - C (Shibazaki)
Fe - Si (Sanloup)
Fe - S (Sanloup)
r_1 (Å) - Nearest Neighbor Distance
2.60
2.58
2.56
2.54
2.52
2.50
0
5
10
15
20
25
30
35
40
Total Impurities in Fe-Alloy (at. %)

Figure 4

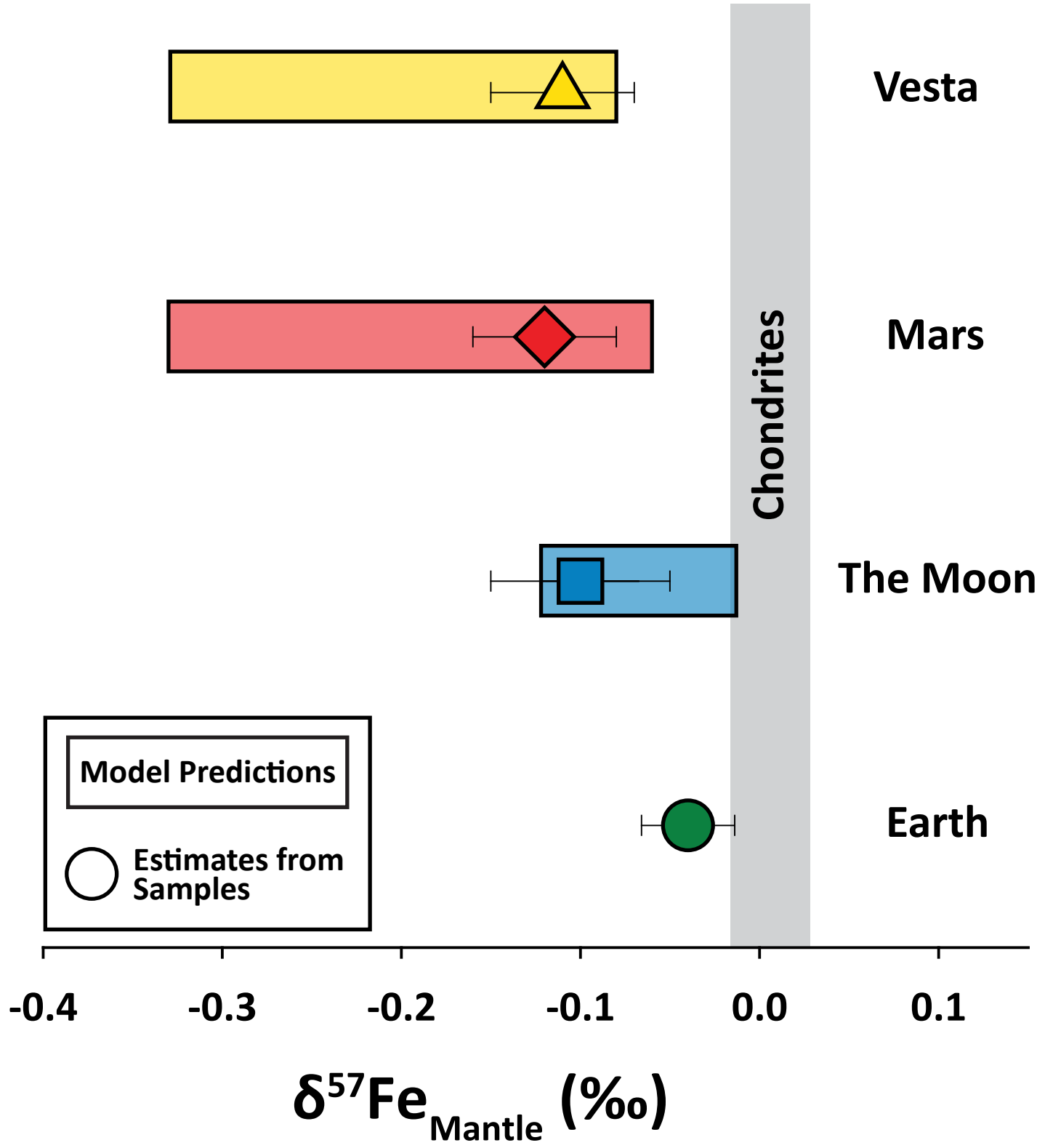
Vesta
Mars
The Moon
Earth
Chondrites
Model Predictions
Estimates from Samples
-0.4
-0.3
-0.2
-0.1
0.0
0.1
δ57FeMantle (‰)

Figure 5

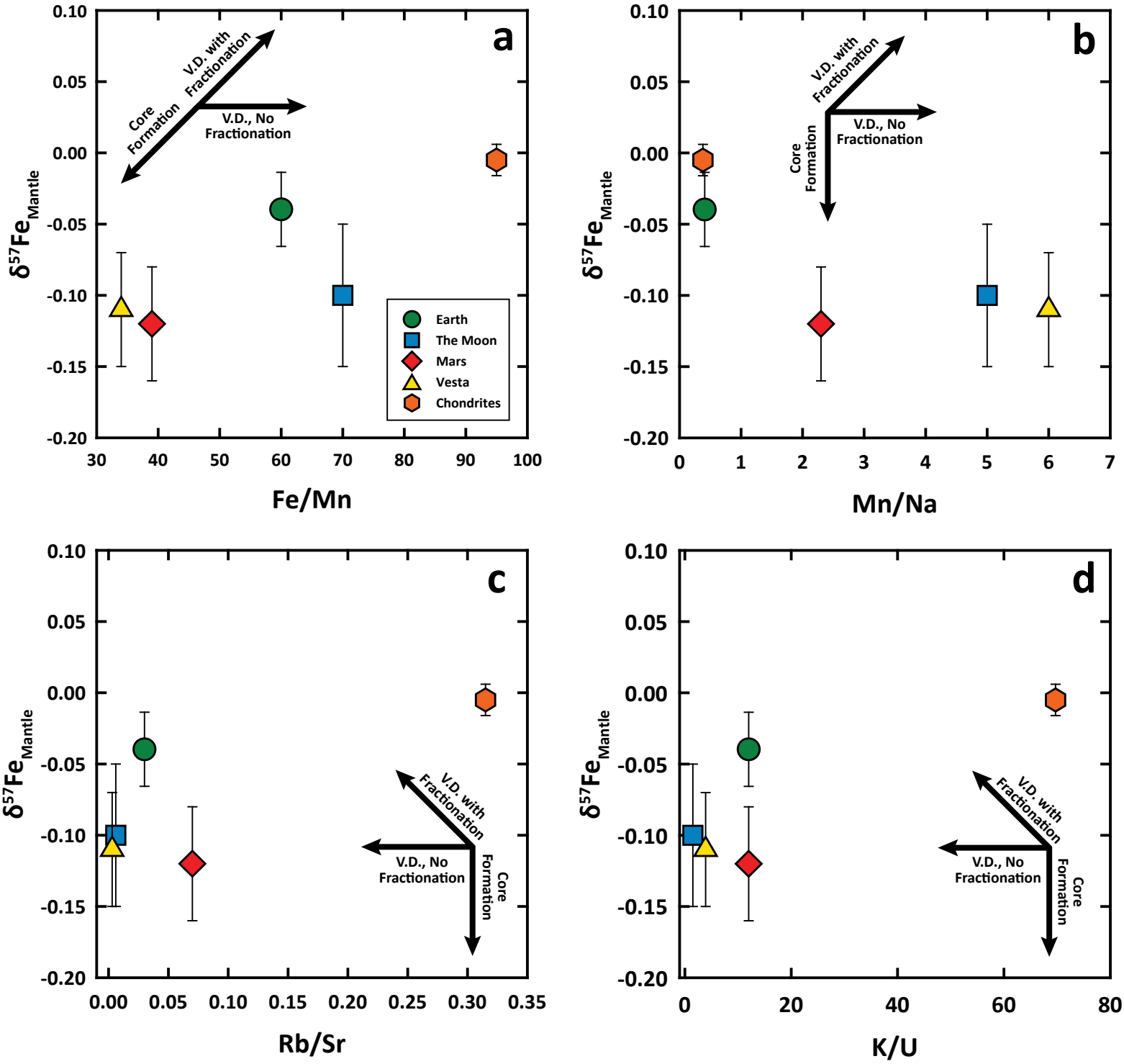
a
b
c
d
$\delta^{57}Fe_{Mantle}$
Fe/Mn
Mn/Na
Rb/Sr
K/U
V.D. with Fractionation
V.D., No Fractionation
Core Formation
Earth
The Moon
Mars
Vesta
Chondrites

Figure 6

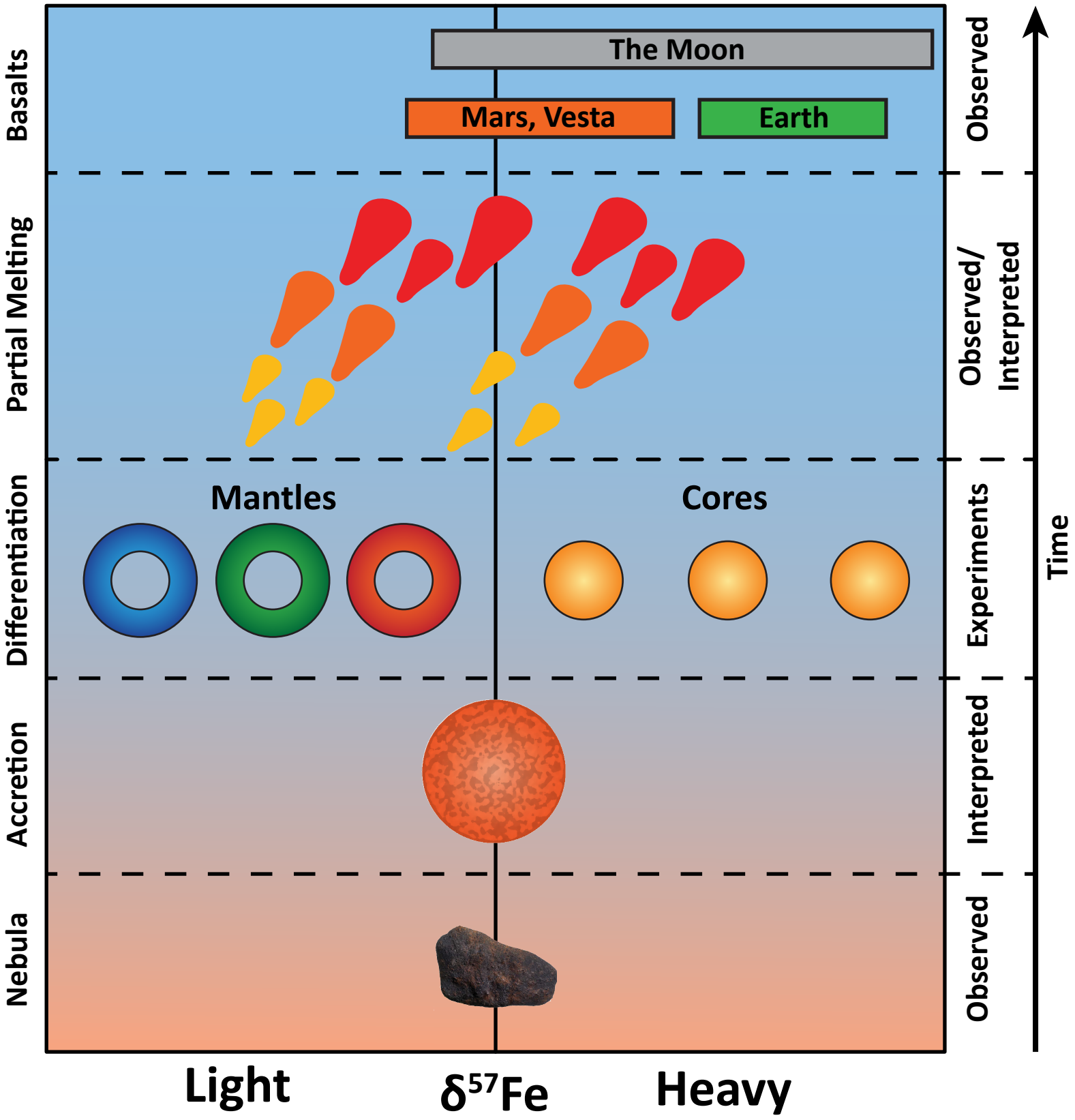
Basalts
Partial Melting
Differentiation
Accretion
Nebula
The Moon
Mars, Vesta
Earth
Mantles
Cores
Observed
Observed/ Interpreted
Experiments
Interpreted
Observed
Time
Light
δ57Fe
Heavy

Figure 7

Table 1: Chemical Compositions of Experimental Run Products

Expt. #	Phase	T (°C)	P (GPa)	Duration (h)	Starting Metal	SiO_2	Al_2O_3	FeO	MgO	CaO	Fe	Si	C_{corr}	Total
PC 1350	Silicate	1850	1	0.5	None	47.56	3.84	5.69	37.07	5.20				99.35
	S. D.					0.55	0.14	0.06	0.62	0.21				
PC 1514	Silicate	1850	1	0.5		51.75	3.59	0.47	35.79	5.33				96.95
	S. D.					0.26	0.01	0.26	0.19	0.02				0.62
	Metal				$Fe_{91}Si_9$						90.3	4.95	4.43	99.70
	S. D.										0.48	0.11	0.54	0.77
PC 1529	Silicate	1850	1	0.5		51.0	3.78	0.60	35.3	5.47				96.89
	S. D.					0.38	0.15	0.05	0.47	0.14				0.65
	Metal				$Fe_{91}Si_9$						90.0	1.40	6.00	97.41
	S. D.										1.23	0.27	1.06	0.72
PC 1567	Silicate	1850	1	2		52.4	3.79	0.75	38.2	5.50				100.65
	S. D.					0.23	0.03	0.03	0.14	0.03				0.39
	Metal				$Fe_{95.5}Si_{4.5}$						93.2	0.87	5.02	99.10
	S. D.										0.58	0.04	0.67	0.97
PC 1570	Silicate	1850	1	0.5		52.3	3.86	0.79	38.1	5.59				100.68
	S. D.					0.29	0.05	0.22	0.11	0.04				0.41
	Metal				$Fe_{95.5}Si_{4.5}$						93.1	0.82	5.85	99.74
	S. D.										0.78	0.05	0.53	0.65
PC 1585	Silicate	1850	1	1		52.7	3.90	0.90	37.9	5.54				100.88
	S. D.					0.43	0.09	0.12	0.28	0.04				0.68
	Metal				$Fe_{95.5}Si_{4.5}$						92.5	0.90	5.98	99.40
	S. D.										0.59	0.10	1.04	1.13

Starting silicate composition (PC 1350) is from Elardo and Shahar (2017)

Values are in wt. %

C_{corr} = Carbon in alloy after correction for C surface contamination

Table 2: Iron Isotopic Compositions of Geostandards and Experimental Run Products

Sample	Phase	n	δ^{56}Fe (‰)	2SE	δ^{57}Fe (‰)	2SE	Δ^{56}Fe (‰)	2SE	$\Delta^{57}Fe_{Metal\text{-}Silicate}$ (‰)	2SE
Geostandards										
AGV-2		14	0.077	0.016	0.129	0.037	-0.010	0.027		
Accepted Values [a]			*0.105*	*0.011*	*0.146*	*0.016*				
BIR-1		16	0.052	0.042	0.054	0.074	0.016	0.027		
Accepted Values [a]			*0.053*	*0.015*	*0.087*	*0.023*				
BHVO-2		14	0.088	0.018	0.191	0.026	-0.042	0.026		
Accepted Values [a]			*0.114*	*0.011*	*0.174*	*0.016*				
Experiments										
PC 1514	Silicate	13	-1.545	0.049	-1.344	0.062	-0.634	0.018	0.072	0.085
	Metal	10	-1.512	0.032	-1.272	0.059	-0.650	0.035		
PC1529[b]	Silicate	11	-2.770	0.029	-2.552	0.048	-1.040	0.030	-0.013	0.054
	Metal	11	-2.765	0.022	-2.565	0.025	-1.026	0.019		
PC1567	Silicate	10	-1.425	0.027	-1.178	0.038	-0.626	0.017	-0.012	0.063
	Metal	10	-1.422	0.025	-1.190	0.050	-0.616	0.036		
PC1570	Silicate	10	-1.400	0.027	-1.230	0.051	-0.566	0.027	0.059	0.061
	Metal	11	-1.366	0.025	-1.171	0.034	-0.572	0.022		
PC 1585	Silicate	19	-1.399	0.014	-1.170	0.028	-0.605	0.026	0.059	0.047
	Metal	20	-1.335	0.017	-1.111	0.038	-0.582	0.026		

[a]Values from Craddock and Dauphas (2010)

[b]A lower metal/silicate in this experiment resulted in more negative δ^{57}Fe values than other experiments